

# A Galaxy-Independent Radial Variable Reveals Universal Dark-Matter Profiles

P. Steffen<sup>1\*</sup>

<sup>1</sup>Deutsches Elektronen-Synchrotron DESY, Hamburg, Germany

\*corresponding author: peter.steffen@desy.de

## Abstract

Standard parametric halo models do not yield a unified description of the dark-matter (DM) distribution in SPARC galaxies, motivating a non-parametric approach to identify common DM properties across systems of different sizes and masses. Assuming that in the DM-dominated regime the baryonic mass enters only through a global scale, we define a galaxy-independent radial variable  $r_{\text{sc}}$  by factorizing the physical radius as  $r = r_0 r_{\text{sc}}$ , where  $r_0$  is determined by the condition  $g_{\text{bar}}(r_0) = 2 \times 10^{-12} \text{ m/s}^2$ .

Using all 2693 rotation-curve measurements from 153 SPARC galaxies, we derive unified radial distributions of observed acceleration, circular velocity, and DM mass. The combined data reveal:

- the onset of DM effects at  $r_{\text{sc}} \approx 0.1$ ,
- with DM dominating the baryonic contribution for  $r_{\text{sc}} \gtrsim 0.2$ ,
- a linear growth of DM mass with radius,  
 $m_{\text{DM}}/M_{\text{bar}} = (6.9 \pm 0.2) r_{\text{sc}} - (0.30 \pm 0.04)$ ,
- a density profile  $\rho \propto r_{\text{sc}}^{-2}$  indicative of an isothermal-like halo,
- and a nearly constant unified rotation velocity for  $r_{\text{sc}} > 0.2$ .

These empirical relations are not apparent in galaxy-by-galaxy rotation-curve fits. They suggest that SPARC galaxies share a common outer-halo structure, providing a model-independent benchmark for evaluating theoretical profiles such as NFW and Burkert and offering empirical constraints on dark-matter halo structure.

# 1 Introduction

## 1.1 Dark-matter halos and the limitations of universal parametric models

The distribution of dark matter (DM) in galaxies has been extensively studied through fits of rotation curves to parametric halo profiles such as NFW, Burkert, Einasto, DC14, and variants of cored or contracted models. Despite decades of effort, these approaches have not converged on a universal halo structure.

A comprehensive SPARC-based analysis by Li et al. (2020) demonstrated this most clearly: after fitting seven widely used halo models individually to 175 galaxies with a full Bayesian treatment of observational uncertainties, they concluded that “the halo mass–concentration relation is not reproduced in detail by any halo model.” This confirms that standard DM halo profiles do not yield the SPARC sample in a unified way.

Subsequent work has reinforced this picture. Analyses allowing non-spherical or triaxial/prolate halo geometries show that even the shape of the dark-matter distribution varies significantly from galaxy to galaxy, preventing any universal description within standard halo parametrizations (e.g. Peters et al. (2021); Sellwood & Sanders (2022)).

Studies incorporating baryon-driven contraction demonstrate that baryonic physics can systematically steepen or modify inner density profiles in ways that differ across galaxies, thereby introducing additional galaxy-to-galaxy diversity (Li et al., 2022).

Other investigations comparing fuzzy dark matter, self-interacting dark matter, and disk+halo composite models to classical cold-dark-matter halos find that none of these parametrized profiles provides a consistently superior fit to the SPARC rotation curves (Bar et al. (2022); Loizeau & Farrar (2021)).

Together, these results indicate that galaxy-by-galaxy parametric halo fits tend to mask large-scale regularities and may therefore not be optimal for uncovering universal features of galactic dark-matter structure.

## 1.2 A unified, galaxy-independent approach

In view of these difficulties, it is natural to ask whether universal features of galactic DM can be revealed only when one avoids parametric assumptions and instead identifies an appropriate galaxy-independent scaling of the data.

In this work, we introduce such a variable: a scaled radial coordinate  $r_{\text{sc}}$  that normalizes the physical radius by a baryonic mass–dependent scale  $r_0$ .

This transformation allows all 2693 SPARC rotation-curve measurements from 153 galaxies to be combined into a single unified radial domain without assuming any particular halo profile.

The SPARC data set has been extensively analysed in the context of galaxy-by-galaxy rotation curve fitting and empirical acceleration relations. The approach adopted here is deliberately different. Instead of modelling individual galaxies, we introduce a baryon-defined, galaxy-independent radial coordinate that allows the combined analysis of all systems without assuming any parametric halo profile. This reveals emergent dark-matter regularities that are not apparent in single-galaxy studies.

### 1.3 Main Results

Using this scaling, we obtain:

- a universal relation between  $r_{\text{sc}}$ , observed acceleration, and DM acceleration;
- a universal DM mass profile, growing approximately linearly with radius;
- a corresponding density profile  $\rho \propto r_{\text{sc}}^{-2}$ ;
- and a nearly constant unified rotation velocity at larger values of  $r_{\text{sc}}$ , consistent with an isothermal-like halo.

These empirical relations are not visible in standard rotation-curve fits. The results suggest that a simple, universal structure underlies the outer dark-matter halos of SPARC galaxies, independent of galactic size, mass, or morphology.

The factorization of the radial galactic distance into the two components — the galaxy-dependent scale  $r_0$  (set by baryonic mass) and the dimensionless radial coordinate  $r_{\text{sc}}$  — is described in Section 2. In Section 3 we investigate unified radial distributions using the 2693 observed data points from 153 galaxies provided by the SPARC collaboration McGaugh et al. (2020). The results are discussed and compared to expectations in Section 4, followed by conclusions in Section 5.

## 2 The Factorization of Radial Distance of Galaxies

### Ansatz:

In the radial domain where dark matter begins to dominate ( $g_{\text{bar}} \gtrsim 10^{-11} \text{ m/s}^2$ ),

we assume that the only dependence on the host galaxy enters through the *total baryonic mass* and the *distance from the center*. This implies that the DM-related physics is insensitive to additional structural properties (e.g. morphology, scale length, gas-star distribution), and therefore the radius can be factorized into a galaxy-dependent scale  $r_0$  and a universal, dimensionless coordinate  $r_{\text{sc}}$ .

McGaugh et al. (2016) analyzed observations of 2693 stellar objects in 153 galaxies and determined the accelerations expected from baryonic mass ( $g_{\text{bar}}$ ) and the observed centripetal acceleration ( $g_{\text{obs}}$ ) derived from circular velocities. They found that averages of  $g_{\text{obs}}$  in bins of  $g_{\text{bar}}$  describe a tight relation between the two accelerations that is independent of galactic type, size, mass, or morphology. They also provided a widely used empirical fit:

$$g_{\text{obs}} = \frac{g_{\text{bar}}}{1 - e^{-\sqrt{g_{\text{bar}}/g_{\text{f}}}}}, \quad (1)$$

valid in the acceleration range

$$10^{-10} \text{ m/s}^2 > g_{\text{bar}} > 2 \times 10^{-12} \text{ m/s}^2.$$

At such low accelerations, the radial distances from galactic centers are so large that only the *total* baryonic mass contributes significantly. In this regime  $g_{\text{bar}}$  serves as a proxy for radius via

$$g_{\text{bar}} = \frac{G M_{\text{bar}}}{r^2}, \quad (2)$$

where  $G$  is the gravitational constant and  $M_{\text{bar}}$  is the baryonic mass of the galaxy.

Equation 1 uses  $g_{\text{bar}}$  as a radial indicator, but Equation 2 shows that  $g_{\text{bar}}$  depends explicitly on  $M_{\text{bar}}$ . Thus two galaxies with identical  $g_{\text{bar}}$  values correspond to different radii if their baryonic masses differ. This prevents a unified radial description across galaxies.

To resolve this, we *factorize* the physical radius as

$$r = r_0 r_{\text{sc}},$$

where  $r_0$  is defined as the radius at which  $g_{\text{bar}}$  equals a reference value  $2 \times 10^{-12} \text{ m/s}^2$ , covering the complete range of the SPARC data:

$$r_0 = \sqrt{\frac{G M_{\text{bar}}}{2 \times 10^{-12} \text{ m/s}^2}}. \quad (3)$$

Using equation 2, the dimensionless scaled radial coordinate becomes

$$r_{\text{sc}} = \frac{r}{r_0} = \sqrt{\frac{2 \times 10^{-12} \text{ m/s}^2}{g_{\text{bar}}}}. \quad (4)$$

Thus: -  $r_0$  represents the *gravitational reach* of a galaxy: the radius where baryonic acceleration becomes negligible. -  $r_{\text{sc}}$  removes the dependence on  $M_{\text{bar}}$  and maps all galaxies to the same normalized radial range.

For all SPARC galaxies, the choice  $g_{\text{bar}}(r_0) = 2 \times 10^{-12} \text{ m/s}^2$  yields a convenient domain

$$0 < r_{\text{sc}} < 1,$$

from the galactic center ( $r_{\text{sc}} = 0$ ) to the edge of gravitational relevance ( $r_{\text{sc}} = 1$ ).

Because  $r_{\text{sc}}$  is directly tied to  $g_{\text{bar}}$ , independent of  $M_{\text{bar}}$ , it provides a natural common radial coordinate for all galaxies. To recover the physical radius of a specific system, one multiplies by its  $r_0$ :

$$r = r_{\text{sc}} \cdot r_0.$$

In addition, unified mass quantities are expressed in terms of scaled mass,

$$m_{\text{sc}} = \frac{m}{M_{\text{bar}}}, \quad (5)$$

where  $m$  is the enclosed DM mass and  $M_{\text{bar}}$  is the galaxy's baryonic mass. This scaling enables a direct comparison of mass profiles across galaxies without dependence on absolute mass normalization.

### 3 The Unified Radial Distributions of the SPARC Data

Observations of 2693 stellar tracers in 153 SPARC galaxies are used to construct unified, galaxy-independent radial distributions. All individual measurements of  $g_{\text{bar}}$  and  $g_{\text{obs}}$  are employed. The logarithmic accelerations provided by the SPARC collaboration were transformed to linear units of  $10^{-12} \text{ m/s}^2$ , which allows a more transparent physical interpretation of acceleration scales and a straightforward treatment of statistical uncertainties.

Figure 1a shows the individual values of  $g_{\text{obs}}$  as red dots for different  $r_{\text{sc}}$  values. They are determined from  $g_{\text{bar}}$  using Eq. (4). The original

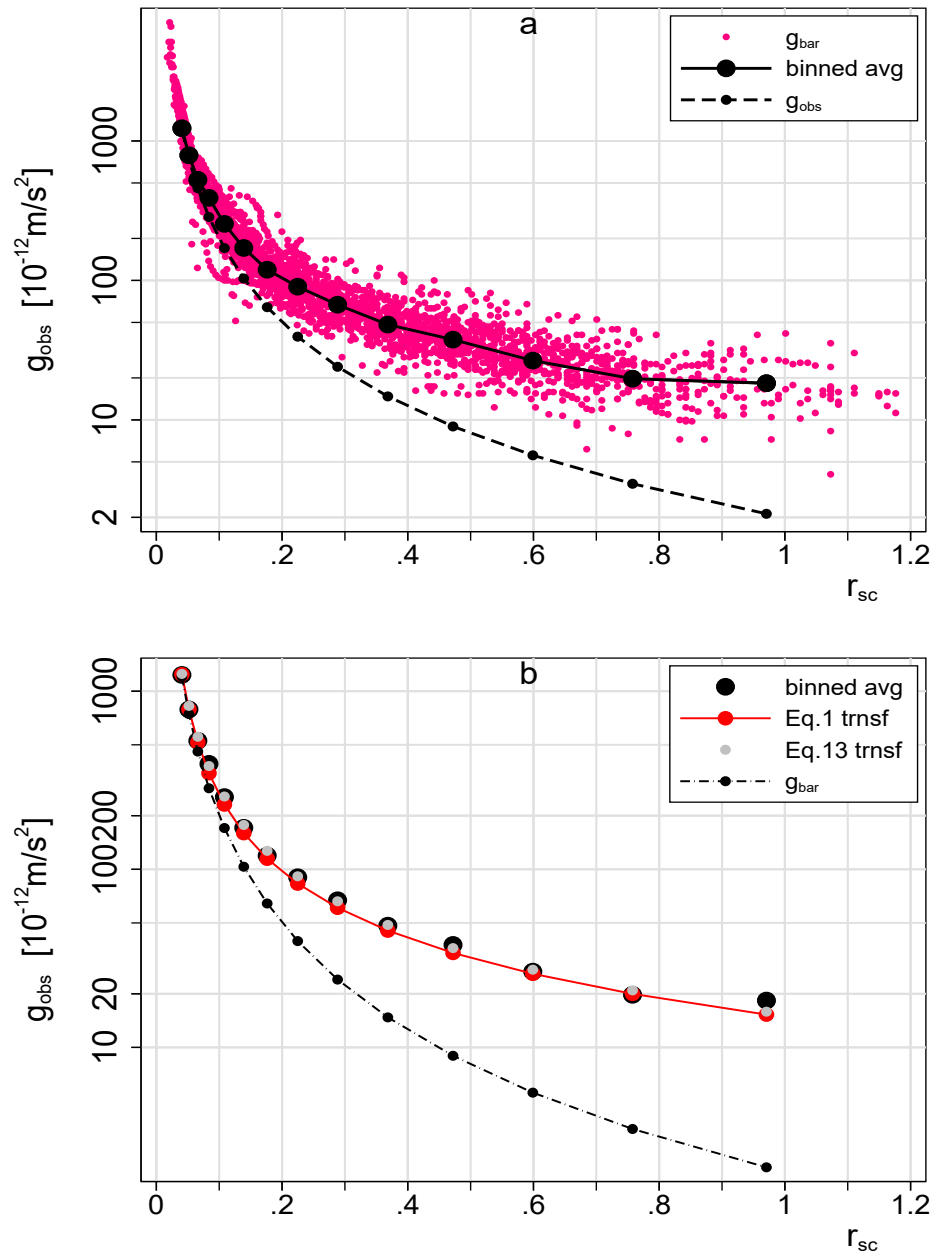


Figure 1: **a:** Distribution of  $g_{\text{obs}}$  values (red dots) and the binned averages (black thick points). Also shown are average values of the  $g_{\text{bar}}$  bins (black points/line).

**b:** Distribution of  $g_{\text{obs}}$  averages (black thick points) and the fit of Eq. 1 (red). Average values of  $g_{\text{bar}}$  are shown as black points and dashed line.

equidistant bins in  $\log(g_{\text{bar}})$  used by McGaugh et al. (2016) were transformed into corresponding  $r_{\text{sc}}$  bins via Eq. (4) and are listed in Table 1.

Bin	$r_{\text{sc}}$ $r_{\text{eff}}$	$g_{\text{bar}}$ $\sigma$	$g_{\text{obs}}$ $\sigma$	$v_{\text{u}}$ $\sigma$	$m_{\text{DM}}$ $\sigma$	$\Delta(m_{\text{DM}}/M_{\text{bar}})$ $\sigma$	$\rho_{\text{DM}}(r_{\text{eff}})$ $\sigma$
1	0.0407 0.0248	1209.43 26.88	1234.37 41.99	6.99 0.04	0.000 0.036		
2	0.0518 0.0491	744.09 11.71	789.58 17.51	6.34 0.03	0.096 0.022		
3	0.0660 0.0629	458.48 6.40	526.92 9.21	5.89 0.03	0.148 0.020		
4	0.0837 0.0802	285.16 3.54	391.06 7.32	5.77 0.03	0.380 0.023	0.133 0.003	85.726 2.155
5	0.1083 0.1026	170.53 1.90	254.37 4.51	5.22 0.03	0.479 0.027	0.176 0.004	52.346 1.316
6	0.1391 0.1314	103.39 1.09	170.96 2.99	4.92 0.03	0.738 0.027	0.221 0.006	31.934 0.803
7	0.1764 0.1684	64.31 0.62	119.40 1.65	4.60 0.03	0.950 0.025	0.290 0.007	19.449 0.489
8	0.2249 0.2156	39.53 0.36	90.23 1.49	4.58 0.03	1.344 0.039	0.363 0.009	11.865 0.298
9	0.2884 0.2762	24.05 0.22	67.00 1.03	4.42 0.03	1.818 0.041	0.475 0.012	7.226 0.182
10	0.3683 0.3536	14.74 0.13	48.26 0.67	4.20 0.04	2.236 0.046	0.596 0.015	4.408 0.111
11	0.4720 0.4510	8.98 0.07	37.64 0.50	4.19 0.04	3.169 0.056	0.750 0.019	2.711 0.068
12	0.5990 0.5771	5.57 0.05	26.63 0.39	4.06 0.05	3.786 0.074	0.992 0.025	1.655 0.042
13	0.7576 0.7375	3.48 0.03	19.74 0.39	3.89 0.06	4.754 0.114	1.226 0.031	1.014 0.025
14	0.9707 0.9709	2.12 0.04	18.33 0.74	4.01 0.10	7.318 0.339	1.983 0.050	0.585 0.015

Table 1: Combined unified variables of  $r_{\text{sc}}$  bins. For each bin, the first line gives the values of the variable, the second line lists the statistical uncertainties; for  $r_{\text{sc}}$  the listed value corresponds to the effective shell radius  $r_{\text{eff}}$ . Accelerations are in units of  $10^{-12} \text{ m/s}^2$ , unified velocities in  $\text{m/s}/\sqrt{r_0}$ , masses in units of  $M_{\text{bar}}$ , and the volume mass density in units of  $M_{\text{bar}}/r_{\text{eff}}^3$ .

For each  $r_{\text{sc}}$  bin, averages of  $g_{\text{bar}}$  and  $g_{\text{obs}}$  were determined using a robust two-step procedure. First, the lowest and highest 5% of values were excluded. In a second step, only data within 2.5 standard deviations of the

preliminary mean were retained. In addition, the median was determined for each bin to control for asymmetric distributions. The resulting averages (with uncertainties derived from the scatter) are shown in Fig. 1a,b as thick black points.

Below  $r_{\text{sc}} \approx 0.10$ , the difference between  $g_{\text{obs}}$  and  $g_{\text{bar}}$  is small, but beyond this radius the deviation increases monotonically. The prediction of Eq. (1) from McGaugh et al. (2016) (converted to  $g_{\text{obs}}(r_{\text{sc}})$ ) is shown as the red curve in Fig. 1b and agrees well with the averages.

Importantly, the unified relations appear only after applying the scaling  $r = r_0 r_{\text{sc}}$ ; in the physical radius  $r$ , the SPARC galaxies do not display a common profile.

### 3.1 Unified Radial Velocity Distribution

The observed centripetal acceleration is related to circular velocity through

$$g_{\text{obs}} = \frac{v_{\text{obs}}^2}{r}. \quad (6)$$

Using  $r_{\text{sc}}$  and  $r_0$ , a galaxy-independent (unified) velocity is introduced:

$$v_{\text{obs}} = \sqrt{g_{\text{obs}} r} = \sqrt{g_{\text{obs}} r_0 r_{\text{sc}}} = v_{\text{u}} \sqrt{r_0}, \quad (7)$$

where  $v_{\text{u}}$  is the unified velocity. Averaged values of  $v_{\text{u}}$  are listed in Table 1 and shown in Fig. 2 (thick black points). For comparison, the velocity expected from baryons alone is shown as black points.

A nearly constant velocity

$$v_{\text{u}} \approx 4.2 \pm 0.3 \quad (8)$$

is observed for  $r_{\text{sc}} > 0.2$ . Using Eq. (4), a relation between  $v_{\text{u}}$ ,  $g_{\text{obs}}$  and  $g_{\text{bar}}$  is obtained:

$$v_{\text{u}} = \sqrt{g_{\text{obs}} r_{\text{sc}}} = \sqrt{g_{\text{obs}} \sqrt{\frac{2 \times 10^{-12}}{g_{\text{bar}}}}} \quad (9)$$

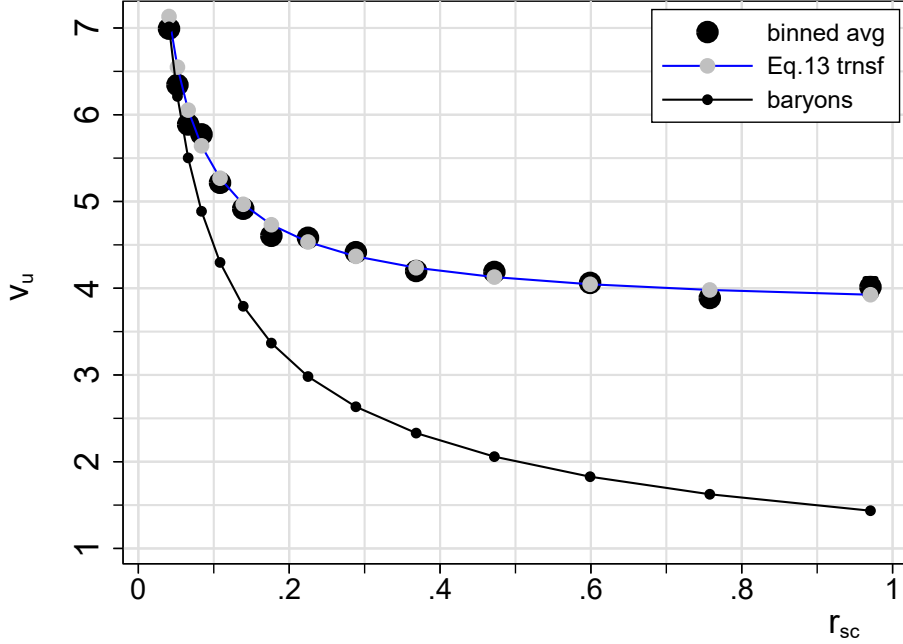


Figure 2: Unified velocities  $v_u$  as a function of  $r_{sc}$  (thick black points). Gray points and blue line show the transformed values from the linear mass fit (Eq. 13). Black points and line show the velocities expected from baryonic mass alone.

Equation 9 follows directly from the definition of  $v_u$  and represents an exact reparameterization of the observed quantities. The empirically observed near constancy of  $v_u$  then implies an approximate correlation between  $g_{obs}$  and  $g_{bar}$ , as reported by McGaugh et al. (2016), rather than an exact functional relation.

Therefore an independent fit is performed which is described in section 3.2. The resulting fit values are transformed to  $v_u$  and shown in the figure. They describe the drift of  $v_u$  quite well for  $r_{sc} > 0.10$ .

### 3.2 Unified Radial Distribution of DM Masses

The DM acceleration is obtained from

$$g_{DM} = g_{obs} - g_{bar}. \quad (10)$$

A division by  $g_{\text{bar}}$  gives

$$\frac{g_{\text{DM}}}{g_{\text{bar}}} = \frac{g_{\text{obs}}}{g_{\text{bar}}} - 1, \quad (11)$$

resulting in the mass ratio enclosed within radius  $r_{\text{sc}}$

$$\frac{g_{\text{DM}}}{g_{\text{bar}}} = \frac{G \cdot m_{\text{DM}}/r^2}{G \cdot M_{\text{bar}}/r^2} = \frac{m_{\text{DM}}}{M_{\text{bar}}}. \quad (12)$$

Observed mass ratios are shown in Fig. 3a as a function of  $r_{\text{sc}}$  as red dots. Averaged values are listed in Table 1 and shown in Fig. 3a and b as thick black dots. The relation is almost perfectly linear for  $r_{\text{sc}} > 0.10$ . A least-squares fit to the medians and the average values with the inverse squared errors as weights results in

$$\frac{m_{\text{DM}}}{M_{\text{bar}}} = (6.93 \pm 0.17) r_{\text{sc}} - (0.25 \pm 0.04) \text{ (med.)}, \quad (13)$$

$$= (7.03 \pm 0.21) r_{\text{sc}} - (0.25 \pm 0.04) \text{ (avr.)}. \quad (14)$$

The residuals show no evidence for systematic deviations and are consistent with statistical scatter, indicating that the linear fits provide adequate descriptions of the data within the observational uncertainties. The DM signal becomes significant only for  $r_{\text{sc}} \approx 0.1$ ; below this threshold, the measurements are consistent with zero. The negative intercept reflects the fact that the fits are applied only for  $r_{\text{sc}} > 0.1$ .

The linear parameters of the two fits agree well with each other, and the constant terms are identical. The fit quality of the observed median values is slightly better as compared to the fit of the observed average values:  $R^2 = 0.995$ (medians) and  $0.992$ (averages), and  $\text{rms}(\text{residuals}) = 0.072$ (median) and  $0.091$ (averages). Therefore the fit of the medians and its corresponding values of other variables is used as reference.

At  $r_{\text{sc}} \gtrsim 0.2$  the DM signal becomes dominant. The fit values are shown in Fig. 3b as blue points and line.

For comparison, the transformed prediction of Eq. (1) from McGaugh et al. (2016) is also shown in Fig. 3b as red points. As the observed averages, they are nearly all lower than the observed averages. Therefore the fitted curve of equation 13 is generally used as reference.

The last two binned points show the largest deviations from the fitted line. They partially compensate each other. The difference is 2.5 and 1.4 standard deviation taking into account the uncertainties of observations and fit, The last bin is based on only 69 measurements across the 153 galaxies, which may introduce a statistical bias. These outer bins dominate the

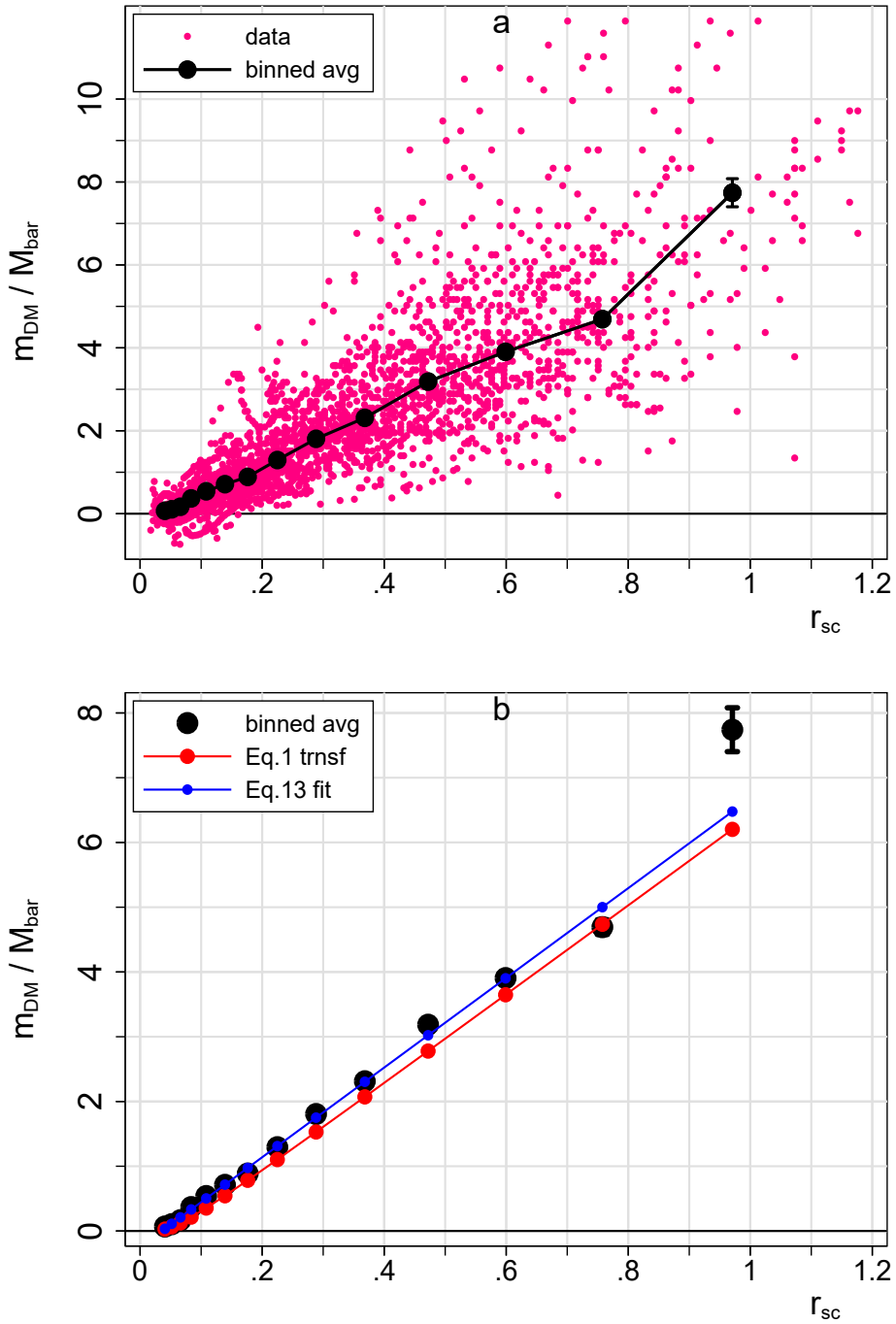


Figure 3: **a:** Observations of DM mass ratios (red dots) and binned averages (thick black points).

**b:** Binned averages (thick black points) and fits from Eq. 1 (red) and Eq. 13 (blue).

contribution to the total dark-matter mass discussed in Sec. 3.4. Future observations with improved coverage at large radii would help to clarify the behavior in this region.

### 3.3 DM Mass and Mass Density in Radial Shells

The linear relation of Eq. (13) implies a differential mass growth:

$$\frac{d(m_{\text{DM}}/M_{\text{bar}})}{dr_{\text{sc}}} = 6.93 \pm 0.17. \quad (15)$$

Thus, the DM mass in a shell between  $r_{\min}$  and  $r_{\max}$  is

$$\Delta \left( \frac{m_{\text{DM}}}{M_{\text{bar}}} \right) = k (r_{\max} - r_{\min}), \quad k = 6.93 \pm 0.17 \quad (16)$$

They are listed in Table 1. The corresponding shell volume is

$$\Delta V = \frac{4\pi}{3} (r_{\max}^3 - r_{\min}^3), \quad (17)$$

resulting in

$$\rho_{\text{shell}} = \frac{k (r_{\max} - r_{\min})}{\frac{4\pi}{3} (r_{\max}^3 - r_{\min}^3)} = \frac{k}{4\pi} \frac{1}{r_{\text{eff}}^2}, \quad (18)$$

where the effective radius is defined by

$$r_{\text{eff}}^2 = \frac{r_{\max}^2 + r_{\max} r_{\min} + r_{\min}^2}{3}. \quad (19)$$

The 3 of the spherical volume ( $4\pi/3$ ) gets absorbed in the definition of  $r_{\text{eff}}$ . Using  $r_{\text{eff}}$  removes the purely geometric bin-width effect that arises when shell densities are parametrized by the mean  $r_{\text{sc}}$ . In this representation the normalization is fixed by the slope  $k$ .

Thus, the linear growth of  $m_{\text{DM}}$  implies an isothermal-like density profile  $\rho_{\text{DM}} \propto r^{-2}$  with a normalization fixed by the slope  $k$ . Propagating the uncertainty of  $k$  (Eq. 15) gives

$$\rho_{\text{shell}}(r_{\text{eff}}) = (0.552 \pm 0.014) r_{\text{eff}}^{-2} \quad (20)$$

in the natural units of the unified coordinate system. The values of  $r_{\text{eff}}$  and  $\rho_{\text{DM}}(r_{\text{eff}})$  are listed in Table 1 and shown in Fig. 4.

Possible additional contributions (constant, linear, or cubic in  $1/r_{\text{sc}}$ ) were tested and found to be consistent with zero within uncertainties; they are therefore omitted in the final representation.

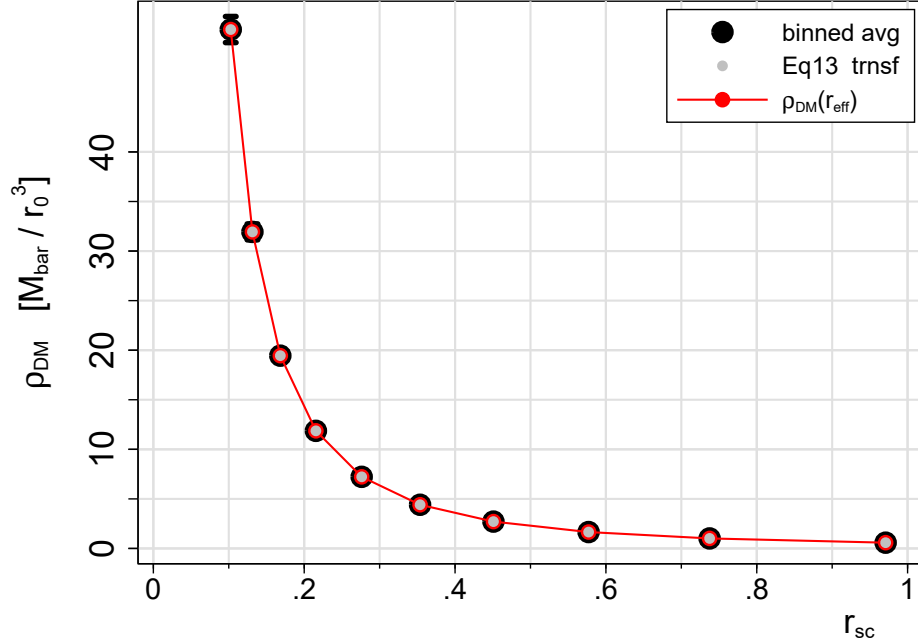


Figure 4: DM density  $\rho_{\text{DM}}$  in shell volumes (thick black points), and  $\rho_{\text{DM}} = (k/4\pi)r_{\text{eff}}^{-2}$  (red points and line).

### 3.4 Total DM Mass Determination

The enclosed DM masses within the spherical volumes are listed in Table 1. The largest accessible volume corresponds to the last bin, giving

$$\left. \frac{M_{\text{DM}}}{M_{\text{bar}}} \right|_{\text{observed}} = 7.32 \pm 0.34. \quad (21)$$

The linear fit of Eq. (13), evaluated at  $r_{\text{sc}} = 0.983$ , yields a lower value,

$$\left. \frac{M_{\text{DM}}}{M_{\text{bar}}} \right|_{\text{fit}} = 6.48 \pm 0.17, \quad (22)$$

where the uncertainty is derived from the parameter errors of the fit.

As noted in Sec. 3.2, the last data point is based on only 69 observations across 153 galaxies, thus, a statistical bias in this outermost bin cannot be

excluded. For this reason, the fit value is taken as the final result:

$$\frac{M_{\text{DM}}}{M_{\text{bar}}} = 6.48 \pm 0.17. \quad (23)$$

## 4 Discussion

The present analysis does not attempt galaxy-by-galaxy modelling, nor does it incorporate detailed baryonic mass distributions or feedback prescriptions. The purpose is instead to identify non-parametric, model-independent properties of dark-matter halos that emerge only when a large ensemble of galaxies is analysed in a unified radial framework.

### 4.1 Empirical Results and Physical Interpretation

Note that the radial range of  $r_{\text{sc}} > 0.10$  covers about 99.9% of the volume of the galactic gravitational reach. All information in this reach is valid for the considered galaxies.

The unified scaling

$$r = r_0 \cdot r_{\text{sc}} \quad (24)$$

enables direct comparison of DM properties across galaxies of different size and baryonic mass. The scale  $r_0$  represents the gravitational reach at which the baryonic acceleration drops to  $2 \times 10^{-12} \text{ m/s}^2$ , while  $r_{\text{sc}}$  provides a dimensionless distance covering the full range of observed accelerations,

$$2 \times 10^{-10} \gtrsim g_{\text{bar}} \gtrsim 2 \times 10^{-12} \text{ m/s}^2.$$

Using 2693 observations from 153 SPARC galaxies, binned in  $r_{\text{sc}}$ , we obtain galaxy-independent distributions of  $g_{\text{obs}}$ ,  $v_{\text{u}}$ , and  $m_{\text{DM}}/M_{\text{bar}}$ . Distance uncertainties, inclination corrections and mass-to-light ratio variations primarily broaden the scatter of the unified relations but do not generate the observed linear dark-matter mass scaling.

The DM acceleration

$$g_{\text{DM}} = g_{\text{obs}} - g_{\text{bar}}$$

becomes significant at  $r_{\text{sc}} \gtrsim 0.1$  and exceeds the baryonic contribution for  $r_{\text{sc}} \gtrsim 0.2$ .

The DM mass profile follows a linear form,

$$\frac{m_{\text{DM}}}{M_{\text{bar}}} = (6.9 \pm 0.2) r_{\text{sc}} - (0.25 \pm 0.04), \quad (25)$$

implying a steady accumulation of DM with radius. Evaluating the linear fit at the maximum sampled radius yields

$$\frac{M_{\text{DM}}}{M_{\text{bar}}} = 6.5 \pm 0.2, \quad (26)$$

slightly above the cosmological value  $\approx 5.5$  inferred from Planck Collaboration (2020). However, the SPARC data extend only to  $r_{\text{sc}} \approx 1$ , therefore this value may be a lower limit.

The unified circular velocity  $v_{\text{u}}$  becomes approximately constant,

$$v_{\text{u}} \approx 4.2 \pm 0.3 \quad (r_{\text{sc}} > 0.2),$$

implying a nearly flat rotation curve. Since  $v_c^2 = GM(r)/r$ , a constant velocity requires  $M(r) \propto r$ , which corresponds to

$$\rho_{\text{DM}}(r_{\text{sc}}) \propto r_{\text{sc}}^{-2}.$$

The density is discussed as a function of the unified radial coordinate  $r_{\text{sc}}$ ; for quantities of the binned shells, the corresponding radial position is given by the effective shell radius  $r_{\text{eff}}$ . A direct fit confirms this:

$$\rho_{\text{DM}}(r_{\text{sc}}) = (0.551 \pm 0.014) r_{\text{sc}}^{-2} \quad (27)$$

Thus both the mass and velocity distributions indicate an isothermal-like outer halo structure common to all SPARC galaxies.

## 4.2 Comparison with Theoretical Density Profiles

The empirical scaling  $\rho_{\text{DM}} \propto r_{\text{sc}}^{-2}$  matches the prediction of a classical isothermal halo (Bahcall & Soneira, 1980; Binney & Tremaine, 2008). Such halos naturally produce flat rotation curves over extended radial ranges.

Navarro–Frenk–White (NFW) halos (Navarro et al., 1997) also exhibit a  $1/r^2$  behavior near their characteristic scale radius  $r_s$ , but deviate to  $1/r$  at small radii and  $1/r^3$  at large radii. The broad interval  $0.2 < r_{\text{sc}} < 1$  in which the unified velocity is flat therefore pushes NFW fits toward low concentrations and a large  $r_s$ ,  $r_s > r_0$ , to reproduce the data.

Burkert halos (Burkert, 1995; Salucci & Burkert, 2000), which feature central cores and a steep  $1/r^3$  falloff, do not develop extended flat rotation curves and do not generate a linear  $M_{\text{DM}}(r)$  relation. They might be compatible only at  $r_{\text{sc}} \lesssim 0.1$ , where the data are sparse.

Overall, both the kinematic and mass-based constraints favor isothermal-like behavior over NFW or Burkert forms for the outer regions of SPARC galaxies.

### 4.3 Implications for Dark-Matter Particle Properties

The stability of rotation curves and the  $\rho_{\text{DM}} \propto r_{\text{sc}}^{-2}$  structure imply a dynamically relaxed DM halo. To maintain such equilibrium, individual DM particles must have velocities comparable to the circular velocity at each radius. Overly light or strongly interacting particles would either evaporate from the potential well or cause dynamical heating inconsistent with the observed flatness.

Thus, the unified halo relations place nontrivial constraints on viable dark-matter particle scenarios: they must be massive, cold, and predominantly collisionless, with gravitational interactions dominating their orbital structure.

### 4.4 Scale dependence and Limits of Applicability

It is instructive to consider the range of gravitational accelerations probed by the present analysis. The characteristic acceleration scale defining the radial normalization corresponds to values that are also encountered in much smaller systems, such as the outer Solar System and the Oort cloud. Nevertheless, no dark-matter component is observed or dynamically required on stellar or planetary scales. This demonstrates that the emergence of the unified dark-matter scaling identified here is not triggered by low acceleration alone. Instead, it requires additional conditions, such as a self-gravitating, collisionless component and long-term dynamical relaxation, which are naturally fulfilled in galactic halos but not in stellar systems. The results therefore point to a genuinely galactic-scale phenomenon rather than a universal modification of gravity.

## 5 Conclusion

By factorizing the physical radial distance of galaxies into a baryonic scale  $r_0$  and a dimensionless DM-related variable  $r_{\text{sc}}$ ,

$$r = r_0 \cdot r_{\text{sc}}, \quad (28)$$

we obtain a unified description of 153 SPARC galaxies that removes galaxy-to-galaxy scaling differences and reveals intrinsic dark-matter (DM) properties.

The main results are:

1. **Onset of DM effects:**  $g_{\text{DM}}$  becomes significant at  $r_{\text{sc}} \gtrsim 0.1$  and exceeds  $g_{\text{bar}}$  for  $r_{\text{sc}} \gtrsim 0.2$ .

2. **Mass growth:** The DM mass grows linearly with radius,

$$\frac{m_{\text{DM}}}{M_{\text{bar}}} = (6.9 \pm 0.2) r_{\text{sc}} - (0.25 \pm 0.04),$$

leading to a total enclosed ratio

$$\frac{M_{\text{DM}}}{M_{\text{bar}}} = 6.5 \pm 0.2.$$

3. **Density profile:** The derived  $\rho_{\text{DM}}(r_{\text{sc}}) \propto r_{\text{sc}}^{-2}$  indicates an isothermal-like halo structure.
4. **Kinematic evidence:** A nearly constant unified circular velocity  $v_{\text{u}}$  for  $r_{\text{sc}} > 0.2$  supports the same conclusion.

These findings imply that most detectable DM associated with SPARC galaxies resides at  $r_{\text{sc}} > 0.1$  and that there is little evidence for a substantial central DM core within the observed region. The results are consistent with an isothermal-like halo, while placing constraints on both NFW and Burkert profiles.

Future observations extending to larger radii or with higher sensitivities would help test the persistence of the  $r_{\text{sc}}^{-2}$  behavior and refine constraints on dark-matter particle properties.

## Acknowledgment

I thank the DESY Directorate and the IT division for their continuous support. I am grateful for the productive discussions with the GRAVI group at DESY, G. Schierholz, U. Martyn, and K. Schmidt-Hoberg. Special thanks go to the SPARC collaboration for providing the astronomical data on which this analysis is based.

## References

- Bahcall J., Soneira R., 1980, *Astrophys. J. Suppl.*, 44, 73  
 Bar N., Blum K., Sun C., 2022, *Phys. Rev. D*, 105, 063015  
 Binney J., Tremaine S., 2008, *Galactic Dynamics*, 2 edn. Princeton University Press

- Burkert A., 1995, *Astrophys. J. Lett.*, 447, L25
- Li P., Lelli F., McGaugh S., Schombert J., 2020, *Astrophys. J. Suppl.*, 247, 31
- Li P., et al., 2022, *Astrophys. J.*, 936, 160
- Loizeau N., Farrar G., 2021, *Mon. Not. R. Astron. Soc.*, 505, 4821
- McGaugh S., Lelli F., Schombert J., 2016, *Phys. Rev. Lett.*, 117, 201101
- McGaugh S. S., et al., 2020, SPARC data release, <http://astroweb.case.edu/SPARC/>
- Navarro J. F., Frenk C. S., White S. D. M., 1997, *Astrophys. J.*, 490, 493
- Peters C. M., Bolejko K. A., Zwaan M. R., 2021, *Mon. Not. R. Astron. Soc.*, 508, 3330
- Planck Collaboration 2020, *Astron. Astrophys.*, 641, A6
- Salucci P., Burkert A., 2000, *Astrophys. J. Lett.*, 537, L9
- Sellwood J. A., Sanders R. H., 2022, *Mon. Not. R. Astron. Soc.*, 517, 1250